RHESSI Imager and Aspect Systems

A. Zehnder[a*], J. Bialkowski[a], F. Burri[a], M. Fivian[a], R. Henneck[a], A. Mchedlishvili[a], P. Ming[a], J. Welte[a], K. Thomsen[a], D. Clark[b], B.R. Dennis[b], G. Hurford[b], D. Curtis[c], P. Harvey[c], D. Pankow[c], and the RHESSI team

[a]Paul-Scherrer-Institut, CH-5232 Villigen, Switzerland

[b]Goddard Space Flight Center, Greenbelt, USA

[c]University of California, Berkeley, USA

ABSTRACT

RHESSI uses nine Rotating Modulation Collimators (RMCs) for imaging, each consisting of a pair of grids mounted on the rotating spacecraft. The angular resolutions range from 2.3 arcsec to 3arcmin. The relative twist between the two grids of each pair is the most critical parameter. It must be less than 20 arcsec for the finest grid. After precision alignment, it is monitored by the Twist Monitoring System (TMS) to a few arcsec. The Sun-pointing must be known better than 0.4 arcsec for the image reconstruction. This is achieved by the Solar Aspect System (SAS), which consists of a set of three Sun sensors. Each sensor is focusing the filtered Sunlight onto a linear CCD. The onboard Aspect Data Processor (ADP) selects the 6 limb positions, which over-define the pointing offset of the Sun center with respect to the imaging axis of the imager. The Roll Angle System (RAS) continuously measures the roll angle of RHESSI within arcmin accuracy. The RAS is a continuously operating CCD star scanner. The time of the passage of a star image over the CCD is recorded and defines the roll angle, comparing its pixel position and amplitude with a star map.

Keywords: X-Ray Imaging, Rotating Modulation Collimator, CFRP structures, Twist Monitoring System, Solar Aspect System, Star Tracker.

1. INTRODUCTION

The primary scientific aim of the Reuven Ramathy High-Energy Solar Spectroscopic Imager (RHESSI) mission is to explore the basic physics of particle acceleration and explosive energy release in Solar flares.[1] It is believed that much of the energy released during a flare is used up to accelerate electrons (emitting primarily X-rays), protons and other ions (emitting primarily gamma rays). The mission is to combine, for the first time, high-resolution imaging in hard X-rays and gamma rays with high-resolution spectroscopy. The RHESSI satellite was launched Feb. 5, 2002 as a NASA SMEX mission with a single instrument on a small spin-stabilized spacecraft in a 600 km high orbit.

The imaging capability of RHESSI is based on a Fourier-transformation technique using a set of 9 pairs of Rotating Modulation Collimators (RMCs), each spaced 1.55m apart (see Figure 1).[2, 3] Radiation transmitted through a grid pair is modulated as the grids rotate with the spacecraft around its axis. The resulting pattern depends sensitively on the radial offset of the radiation source from the rotation axis and its spatial extension. The different grid pairs have different slit widths, the corresponding angular resolutions extends from 2.3 arcsec to 3arcmin, allowing sources to be imaged over a wide range of angular scales.

The big advantage of this imaging concept is the fact that the detectors recording the oscillating radiation pattern behind the grid pairs need not be position-sensitive and can thus be optimized for energy resolution. RHESSI is utilizing 9 Ge-detectors.[4] The detectors are cooled to about 80 K by a single-stage, integral Stirling cycle cooler. Information on the energy and arrival time of every single photon will be recorded and transmitted to ground. For the image reconstruction a precise knowledge of the momentary pointing of the imager is required. The polar angle of the imager axis to the Sun center is provided by the Solar Aspect System (SAS)[5] and the roll angle with respect to the heliocentric y-coordinate is provided by the Roll Aspect System (RAS).[6] Thereby each photon event can be corrected for momentary radial displacement and roll angle offset. In this way photon samples with high statistics can be produced leading to an overall spatial uncertainty in the range of arcseconds. The aspect knowledge allows correlating the RHESSI results with results of measurements at other wavelengths, which is the only way to fully understand the nature of the flare energy release in detail.

* Send correspondence to alex.zehnder@psi.ch

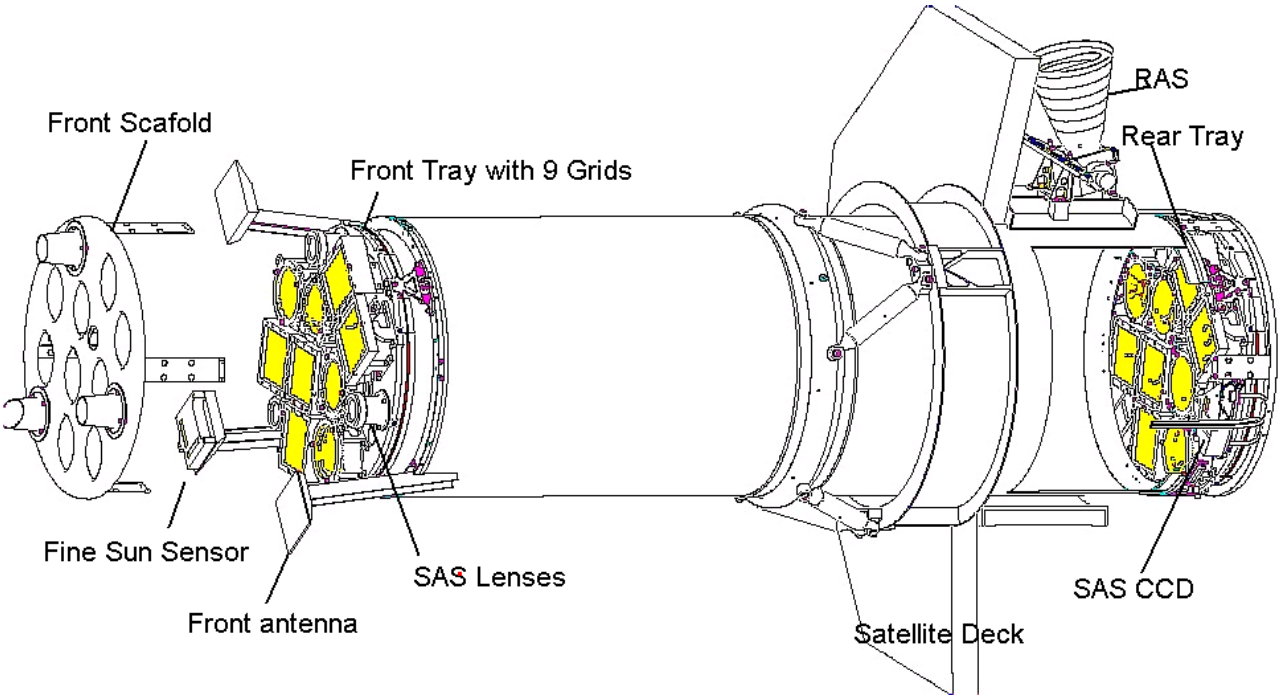

Figure 1: Layout of the imager

Since the pointing of the imager axis is known to better than 1 arcsecond for each photon, the spacecraft attitude control must only be known on the level of arcminutes to ensure that the full Sun is in the field of view of the SAS. However the internal alignment of the imager and the stability of the 9 grid collimators and of the aspect systems RAS and SAS are very high. A relative twist of the order of the ratio pitch/grid diameter reduces the modulated amplitude to almost zero. Thus, the grid pairs must be well aligned in twist during the environmental test and throughout the mission. A ground support equipment for measuring the twist of the system, the twist monitoring system (TMS), was built[7] for the environmental tests

The RHESSI instrument was built by an international collaboration headed by the Space Sciences Laboratory of the University of California, Berkeley with main contributions from NASA Goddard Space Flight Center, Greenbelt, and the University of Delft, Netherlands. Spectrum Astron, Phoenix (AZ), built the spacecraft. The Paul Scherrer Institut (PSI) was responsible for the mechanical imager structure, the alignment of the grids, the Twist Monitoring System (TMS), the Solar Aspect System (SAS), the Roll Angle System (RAS), and the Aspect Data Processor (ADP). The present paper gives an overview of the hardware built at PSI.

2. IMAGER MECHANICAL OVERVIEW

2.1. Requirements and Outline

The principle of the RHESSI imaging is given in detail in Ref. 8. In the context of the present paper we therefore present only a very brief outline based on Figure 2 below. A pair of widely separated grids in front of a cooled Ge-detector produces the characteristic intensity modulation. Each grid consists of a planar array of equally spaced, X-ray-opaque slats separated by transparent slits. If the slits of each pair of grids are parallel to each other and if their pitches (p) are identical, then the transmission through the grid pair depends on the direction of the incident X-rays. For slits and slats of equal width, the transmission is modulated from zero to 50% and back to zero for a change a = p/L , where L is the separation between grids (see Figure 2). The angular resolution is then defined as p/(2L). Mounting the instrument on a rotating spacecraft modulates the transmission of the source photons through the grids.

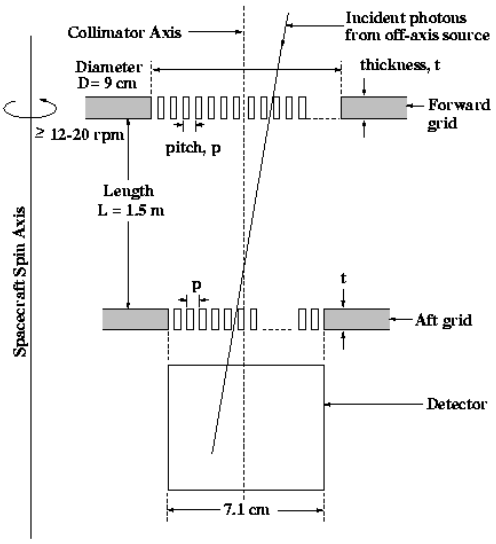

Figure 2: Schematic of one RMC system, showing the parameters that define the imaging capability.

For RHESSI the separation between grids in each RMC is L = 1.55m, the grid pitches ranging from 34μm to 2.75mm in steps of $\sqrt{3}$. This gives angular resolutions that are spaced logarithmically from 2.3 arcsec to ~3arcmin, allowing sources to be imaged over a wide range of angular scales. The thickness ranges from 1.2mm Molybdenum for the finest grids to 30mm Tungsten for the coarsest grids.

A detailed error analysis of the imaging performance has been carried out[9] and the critical engineering requirements for the imager are: Aspect Error in rotating frame=0.5 arcsec, in inertial frame 1arcmin, and relative twist for finest grid pair <20 arcsec. Changing the separation (L) between grids or displacing the grids parallel to the slits has little effect on the imaging performance. A relative displacement perpendicular to the slits affects the phase but not the amplitude of modulation.

Any such displacement will be accurately monitored by the SAS, and is fully compensated in the image reconstruction process. The critical alignment requirement is associated with the rotation or twist of one grid with respect to the other about the line of sight to the source. A relative twist of ratio p/D (D=diameter of grid=90mm) reduces the modulated amplitude almost to zero. Thus, the grid pairs must be well aligned in twist throughout the mission for two reasons:

- twist represents the major contribution of the error to the source location accuracy
- maintaining maximum contrast; e.g. the twist mentioned before produces a 5% loss of the nominal contrast.

Thus, the critical alignment requirement for the imager structure is to maintain the relative twist to within 20arcsec under flight conditions for at least two years. Apart from the problem of launch, vibrations this also includes temperature variations between 0°C and 40°C and the fact that material outgassing in vacuum should not introduce twist.

The approach we used to achieve this goal was to develop a very stable structure and a precise, easy-to-use optical system to measure the relative twist for all grid pairs individually and between the grid-supporting trays (the Twist-Monitoring-System, TMS) during the whole qualification phase. From the history of these TMS measurements, supported by additional measurements with Coordinate Measuring Machines (CMM) and specific tests to verify the stability under enhanced humidity and in vacuum we concluded that no active in-flight re-alignment is necessary. In-flight monitoring of the relative twist between the grid trays will be possible with the SAS, based on the careful ground- and in-flight calibration of the SAS.

The dimensional constraints given by the desired spatial resolution, the size of the Ge-detectors, and of the launch vehicle (Pegasus) resulted in a maximum grid separation L = 1.55 m and a diameter of 46 cm for the imager tube. Figure 1 shows the whole imager with its main components. They are discussed in the following sections.

2.2. Imager Tube

The main imager structure consists of a Carbon-Fiber Reinforced Polymer (CFRP) tube with Titanium end and center rings. The winding layout of the CFRP tube has been optimized in order to maximize form stability in variable environmental conditions. Titanium closely matches the coefficient of linear thermal expansion of CFRP. On the end rings the grid bearing trays are mounted.

A tube with an inner diameter of 460mm was produced by filament winding in a symmetric lay-out with the following laminate sequence and ply thickness: $\pm 86^{o}$ (0.47mm), $\pm 45^{o}$ (0.445mm), $\pm 12^{o}$ (0.89mm), $\pm 45^{o}$ (0.445mm), and $\pm 86^{o}$ (0.47mm), with a total thickness of 2.72mm. Fibers are high strength, standard modulus type Toray T-300B 50B 6K, resin ACE 1010 (Ciba Geigy LY556 / HY917 / DY070). The Bauweisenlabor of the ETH in Zürich measured the fiber content to be 65.3 %, and the interlaminar shear strength to be 43.8 N/mm^2. The worst-case calculations yielded 0.169 arcsec/^{o}C twist.[10] The actual production of the CFRP imager tube was done by ACE in Fredericia, Denmark.

With the available mandrill a CFRP tube was originally produced that was more than twice the required length for the flight model imager. A first part of 1400mm length was used for assembling a fully representational Qualification Model (QM) tube, which was extensively used as a test bed before producing the flight model (FM) from the remainder of the CRFP structure. Immediately after curing, the CFRP tube was subjected to a thermal aging procedure consisting of five cycles between -20 and +40^{O}C to relieve residual stress.

The interface between the spacecraft instrument deck and the telescope is defined by three titanium mounting blocks to which six Glass-Fiber Reinforced Plastic (GFRP) struts are supporting the imager. The GFRP parts were produced by wet-winding at the ETH Bauweisenlabor in Zürich. Titanium end fittings were bonded to the GFRP tubes with Hysol EA 9303.3 NA adhesively. In a mechanical pull test a strut fitting yielded at 50 kN, shearing off the titanium cone (TiAl6Va4) on the fitting (cross section of 1 cm^2). Neither the GFRP strut nor the bonding showed any sign of damage.

The center and end rings were bonded to the CFRP tube; they were produced from TiAl6Va4 to avoid a mismatch in the thermal expansion of the materials. The rings for the flight model were perfect in their shapes to within a few micrometers, as single pieces and also after bonding to the tube. Glues used were Ciba Geigy Araldite AV138/HV998 for the end rings and 3M Scotch Weld 2216 B/A for the center ring, respectively. In-process samples demonstrated sufficient bonding strengths of between 14.6 and 18.6 N/mm^2.

2.3. Trays and Tray Mounts

On each end of the telescope tube a tray bears the individual grids. To support the trays on the end rings, kinematic tray mounts were developed at PSI. They firmly hold the trays at three points and ensure a perfect fixture flexible in the radial direction while not over-constraining any degree of freedom. Each tray sits on two fixed mounts and one adjustable mount. All are designed with the same stiffness. The adjustable mount allows to fine-tune the orientation of a tray by providing tangential translation over a range of up to several 100 micrometers at one mounting point. The stability of the adjustment has to be guaranteed to 10 micrometer at the most and actually appears to be significantly better, as about the same as the resolution of the twist monitoring system.

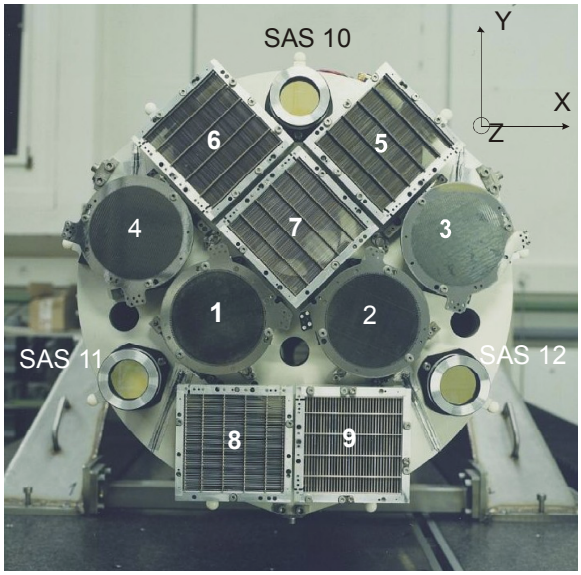

Figure 3 RHESSI front tray with 5 square grids, 4 round grids and the three SAS lenses

The trays are made of a special aluminum alloy (AlMg4.5Mn) that was chosen for easy machining and welding. The same time the material should not creep. The trays are hollow, electron beam-welded-from two parts to provide the required stiffness at an acceptable mass. To release residual stress after production of the trays are tempered in a moderate heat treatment, warming and cooling them for several hours from –20^{o}C to 330^{o}C. The final grid-bearing surfaces of the trays are lapped to a flatness of 2μm rms. The rear surface of the front tray facing into the imager tube is coated with a black thermal paint to enhance temperature equilibrium between trays.

The grids, the SAS and the TMS units are mounted with M4 screws into threads rolled into the 4mm thick front sheet of the trays. Extensive pull-out tests showed that one such thread torqued with 4Nm can be loaded with 4000 N.

Nine 0.5-inch diameter sapphire tooling balls define the reference coordinate system of each tray. They are spring-mounted on the periphery of the tray with 40 degree spacing, starting at the +y axis (see Figure 3). Both grid trays are thermally controlled to a temperature of 20(3)°C. The environmental testing took place in the range 0 to 40°C.

2.4. Grids and Grid Mounts

The design, fabrication and characterization of the grids and mounts are described in detail in Ref. 11. To maintain alignment following thermal and vibrational stresses, flexible elements are used to mount the fine round grids 1 to 4 to the trays, allowing for precision alignment in twist as well. The coarser square grids 5 to 9 were mounted with aluminum blocks, the alignment assured by means of fitting pins with no adjustment possibilities foreseen. To minimize the effect of thermal expansion of the trays, the slats of the fine grids 1 to 4 are radially oriented (see Figure 3).

Grids have fiducial marks, i.e. 30μm pinholes, which are accessible to the optical measuring machine.

2.5. Twist Monitoring System (TMS)

Maintaining the angular alignment of the trays and the grids is essential for the success of the mission. The Twist Monitoring System (TMS) monitors any deviation from the initial alignment using high- precision mechanical and optical Coordinate Measuring Machines (CMM). The TMS is used after transportation of RHESSI and before and after every environmental test.

A total of 10 TMS have been designed, namely one for each grid pair 1 to 8 and two redundant for the tray-to-tray twist. Each individual TMS consists of four pinholes on the rear tray system, each illuminated by a 3mW at 635nm diode lasers, and of two annuli mounted on the front tray and grids (see Figure 4). The pinholes are 30μm in diameter and the annuli have an outer/inner diameter of 3.0/2.8mm and 8 spokes. The 4 pinholes are grouped in 2 pairs (1/2 and 3/4 pair) with spacing of 4.5mm. The distance between the mean of the 1/2- to the 3/4 pinhole pairs and the distance of the centers of the two annuli are chosen in such a way that the four laser rays intersected on a CCD camera (Sony 1/2" CCD chip) 1300mm in front of the front grids (see Figure 4). The camera is mounted on a computer controlled x-y scan table. The exact position of the pinholes and the center of the annuli are measured on an optical CMM with respect to the slat orientation, to the SAS lenses and SAS CCDs to about 1μm precision. Using this information, the expected TMS pattern on the CCD camera can be calculated.

For a TMS measurement the 4 laser diodes behind the pinholes are switched on individually, the diffracted light illuminates the annuli in the front grids or tray. The 1/2 pinhole pair illuminates annulus 1, the 3/4 pinhole pair annulus 2, respectively. The light is further diffracted by the annuli into a Bessel function pattern and recorded individually by the CCD-camera. The center of each 2-d Bessel function pattern is fitted with less than a 1-μm accuracy. Comparing these four patterns with the ones calculated from the CMM measurements any possible twist is detected with redundancy. The resolution of the TMS is in the order of a few arcseconds, i.e. well below the required accuracy.

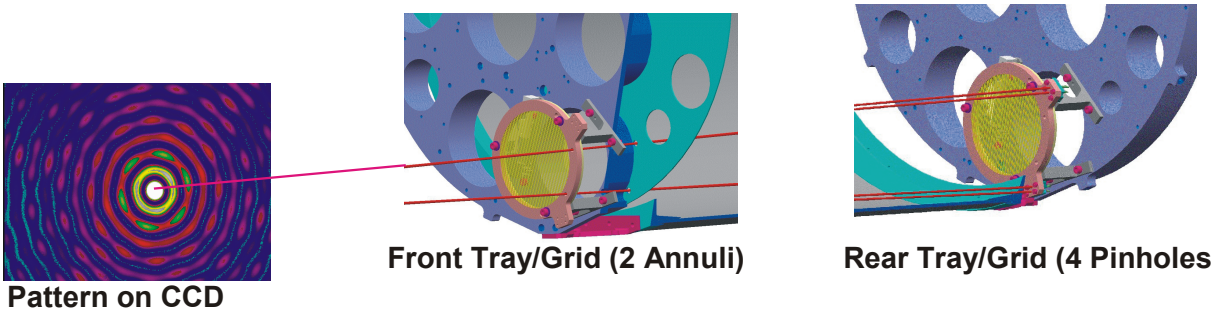

Figure 4: Principle of the TMS (grids or tray): Right side: rear tray/grid with 4 laser diodes attached to four 30 μm pinhole. Middle: Front tray/grid with 2 annuli. Left side: The 4 converting rays are intersected on a CCD camera, producing 4 interference patterns (one shown).

2.6. Alignment of Imager

The alignment of the imaging system was a very crucial task for the success of the mission. It was performed as follows:

1. Characterization of the grids at GSFC, namely determination of the average slats direction to the sunny-side fiducial pinholes (3 per grid, e1, e2, e3).
2. Determination of the individual Tray Coordinate System (TCSi, i=R or F) defined by the nine tooling balls at the periphery of the front and rear tray on a mechanical and optical Coordinate Measuring Machine (CMM) Mitutoyo at the ETH of Zurich. The optical to mechanical measuring system was cross-calibrated frequently. The deviations were always less than 2μm. The trays were placed horizontally adjacent to each other.
3. Determination of the position of the individual fiducial marks on the grid and the TMS features (Rear pinholes, front center of annuli). Calculation of slat directions of the individual grids in the TCSi.
4. If needed twist alignment of grids on front and rear tray by the adjustable mount.

5. Re-measurement of the grid fiducals and determination of the position of the tray TMS, of the 3 SAS lenses on the front tray and the position and orientation of the 3 SAS CCDs on the rear tray.
6. The trays were mounted on the imager tube and a coarse adjustment was made with the tray TMS. For the final tray to tray alignment the imager was placed horizontally on the PSI CMM. At least seven out of nine tooling balls around the circumference of the trays were accessible to a mechanical touch probe.
7. Series of full TMS measurements were made immediately after the alignment procedure with the imager in horizontal and vertical position.

All the measurements were done repeatedly (at least 3 times). The agreement between the different measurements was always better than 3μm rms. Possible twist misalignment due to gravitational effects was tested with dummy grids with various weights; the effects were well inside the required 20 arcsec. The shrinking and twisting due to out-gassing of the imager CFRP in space could be another possible source of misalignment. Extensive vacuum tests were made with the identical QM imager; the results are given below.

Finally, the Imaging Coordinate System (ICS) was defined as follows: the origin was set to the center of gravity of the mid-position of the 3 SAS CCD's on the rear tray, the +z direction was defined by the center of gravity of the optical centers of the 3 SAS lenses on the front tray, and the +x direction was defined by the mean zero degree of the rear tray tooling balls.

For completeness, Table 1 gives the relevant position of the front and rear grids including the phase shift measured at GSFC using grid characterization facility. The distance of the centers between the front tray to rear tray is 1549.878mm. The grid mounts were shimmed in such a way that sunny side surface of the grids are on equal height.

Table 2 gives the Coordinates of SAS system in the imaging coordinate system. The x, y position of the lenses includes the measured shift from the geometrical to the optical center of the lenses and the CCD x, y position includes the shift of the light pass due to the tilt of the optical filter in front of the CCD.

Front Tray	Slat Angle [Degree]	x [mm]	y [mm]	Rear Tray	Slat Angle [Degree]	x [mm]	y [mm]
Grid 1	-157.4322293	-79.0487	-15.6584	Grid 1	-157.4328658	-79.0765	-15.9275
Grid 2	157.5677657	78.6054	-15.9443	Grid 2	157.5665991	78.4801	-15.8094
Grid 3	-157.4192487	139.0254	77.6713	Grid 3	-157.4206437	138.7710	78.1515
Grid 4	157.5413617	-145.6225	74.1294	Grid 4	157.5418078	-145.8835	73.8356
Grid 5	-135.0532286	62.3767	158.4420	Grid 5	-135.0644978	60.6944	160.2225
Grid 6	135.0126327	-62.0260	158.7697	Grid 6	135.0193924	-62.3917	158.7046
Grid 7	45.0400573	21.3602	35.9532	Grid 7	45.0384480	21.0677	35.8931
Grid 8	0.0821078	-56.5347	-176.6893	Grid 8	0.0791066	-56.3194	-176.4613
Grid 9	90.0685218	83.2769	-149.8943	Grid 9	90.0088834	83.1315	-149.7597

Table 1: Coordinates of the rear and front grids in the imaging coordinate system. The x, y position includes the phase shift measured at GSFC using grid characterization facility. The error of the x, y positions is about 2μm and of the slat angle is about 4 arcsec (0.0012^{o}).

Item	x [mm]	y [mm]	z [mm]	CCD Angle[Degree]
CCD 10	-0.2212	182.1646	-0.0583	-179.7549
CCD 11	-157.7104	-91.3780	0.0125	-59.5286
CCD 12	157.9316	-90.7865	0.0458	60.1848
Lens 10	0.2715	182.0173	1546.5278	
Lens 11	-157.7825	-90.7808	1546.0583	
Lens 12	157.5110	-91.2366	1547.0090	

Table 2: Coordinates the SAS in the imaging coordinate system. The x, y position of the lenses includes the measured shift from the geometrical to the optical center of the lenses.

3. RHESSI ASPECT SYSTEMS

3.1. Motivation

Although spacecraft pointing for RHESSI cannot be maintained on an arcsec-level accuracy, arcsecond-class images can still be obtained if the actual instrument pointing is known over longer observation periods with sub-arcsec accuracy and if exact timing of each observed photon could be achieved. Introduction of this information into the whole image

reconstruction procedure then allows to correct for momentary spacecraft misalignment and to recover the nominal spatial resolution.[8] Spacecraft attitude control to within 10arcmin is maintained by a combination of fine Sun sensors, magnetometers and torque rods. Two precise aspect systems are implemented to provide continuous, arcsecond-class aspect knowledge: (a) the Solar Aspect System (SAS) which will yield sub-arcsec knowledge of the radial pointing offset with respect to the Sun center and (b) the Roll Angle System (RAS) which will provide precise knowledge on the roll angle of the rotating spacecraft.[6, 12] Because of the fast rotation (15 rpm) the RAS must operate with integration times that are much shorter than the one of standard star tracking systems. The requirements imposed by the RHESSI image processing called for a custom-made SAS. In the following we describe the SAS design and implementation. Brief descriptions of the SAS have appeared in Refs. 5, 12.

3.2. Solar Aspect System (SAS)

The SAS accuracy is driven by the requirement that momentary pointing misalignment should not degrade the nominal resolution. The uncertainty of the momentary spacecraft pointing yields the dominant single contribution to the spatial resolution[8] and should thus be reduced to <0.4 arcsec error at the 1 σ level. The relative pointing should be continuously available in order to build-up the momentary aspect solution for any photon observed.

The SAS must be able to operate as a real-time Sun sensor as backup for the standard fine Sun sensors. This means that real-time attitude coordinates must be calculated and fed to the spacecraft ACS in order to generate an error signal.

3.2.1. SAS: Principle of Operation

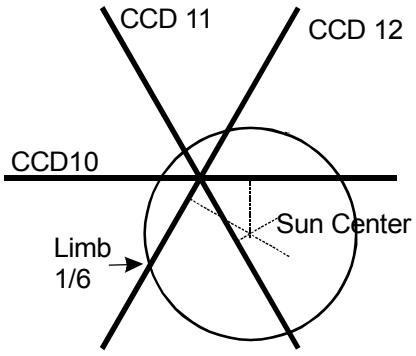

Figure 5: Principle of the SAS operation. For didactical reasons, the 3 CCD were moved to intersect at their centers

The SAS consists of a set of 3 identical lens/sensor subsystems (spaced at 120°) which interface with the spacecraft computer via the Aspect Data Processor (ADP). Each subsystem consists of a lens of 4 cm diameter located on the front grid tray of the imager tube that focuses a solar optical image onto a 2048-element 13x13μm^2 linear CCD located on the rear grid tray (focal length 1.55m). Figure 5 shows a schematic illustration of the SAS principle of operation. The plate scale is 1.73arcsec/pixel and the FOV (i.e. where 2 limbs are visible per CCD) is 14arcmin. Simultaneous exposures of the solar images are made at max 128Hz, programmable from 8Hz in steps of power of 2. For each image there are two locations (limb crossings) where the solar image intersects the CCD. A digital threshold algorithm is used to select N pixels that span each solar limb for inclusion in the telemetry. Determination of the crossing of the 6 limbs locations provided by the 3 subsystems defines the position offset of the Sun in the rotating frame (see Figure 5.)

An unambiguous aspect solution at a given time can be derived from any 2 SAS pairs, yielding 3 independent solutions. Differences between these solutions can be traced back to variations of the positions of the lenses and of the CCDs. The internal consistency of the final solution can be checked by looking at several control parameters and their time derivative. For instance, the inferred solar radii should be independent of pointing direction.

The SAS can also be used as a real-time Sun acquisition sensor to back-up the RHESSI fine Sun-sensor. Since the SAS should provide information to correct the grid-produced images for momentary misalignment, the co-alignment among the different grids and with the SAS must be highly stable and known to within arcseconds.

CCD Field of view [arcmin]	59
Lens (3x)	Fused silica, plano-convex, focal length 1550mm, f/41
Bandpass filter on lens (3x)	Reflective, Si-SiO, ion-plated, center wavelength 670 nm, 12 nm FWHM, peak transmission 1.5%, AR coating
Blocking filter (3x)	Reflective, Si-SiO, ion-plated, blocks between 350 to 1300 nm, AR coating
Sensor (3x)	Linear CCD, Loral-Fairchild 145 EDC, 2048 x (13 x 13) μ^2, 26.6mm
Signal resolution	10 or 8 bit S/W selectable
Plate scale	1.73 arcsec/pixel or 0.133 arcsec/μm
Operating FOV	High accuracy mode (2 limbs/ image): 14arcmin radially
Sun center determination	$\leq$ 0.4 arcsec (1σ) from analysis of 3 subsystems, in flight better than 0.2 arcsec

Update rate [Hz]	≤ 128Hz
Integration time [ms]	0.016 to 2, selectable in steps of 0.016ms
Power consumption [W]	1.2 W/ subsystem, +14V, +12V, +5V
Operating modes	Full image mode, limb mode, attitude-control mode
Operating temperature [°C]	10 °C to 30°C
Spectral sensitivity [nm]	Bandpass 670 nm, 12 nm FWHM
Radiation hardness	≥ 10krad, 100MeV protons

Table 3: Summary of SAS main characteristics

3.2.2. Design of SAS

The SAS is mounted on the imager tube - the lenses on the front grid tray and the CCD sensor and front-end electronics on the rear grid tray. For reasons of stable co-alignment with the grid systems both the lens planes and the sensor planes are placed at the same height and with the same spacing as the grid systems. Extreme care was taken to provide for a mechanically and thermally stable positioning of the grids and of the SAS elements. The critical lateral positioning is ensured by tight tolerances on the mounting pins and on no-slip precautions at the bolt interfaces. This has been tested during several vibration test at imager and full spacecraft level.[13]

3.2.2.1. Lenses and Filters

Each lens (plano-convex, focal length 1.55 m) is made[14] of fused silica and mounted in such a way as to allow for a precise determination of its optical center with the mechanical sensor of a coordinate measuring machine. The lenses are fixed in a special spring-loaded aluminum mount that was re-machined after insertion of the lens so that the optical center coincided with the center of the circumference of mounting ring to within 2 μm. During machining the positional stability of the lens was monitored with a CCD camera. Since the positions of the CCDs and of the fiducial marks of the grids were also measured with micron accuracy, we know the SAS viewing directions with respect to the individual grid pair viewing directions on a level of 1 arcsecond. The focal lengths of the lenses were measured with a relative accuracy of 0.3mm and individual spacers were implemented to provide the correct focal length for each SAS within 0.05mm.

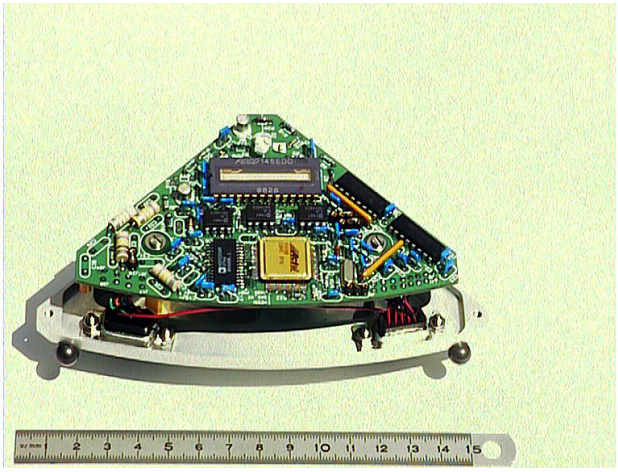

Figure 6: Photograph of the SAS front-end electronics with its cover taken off. The positions of the two tooling balls are measured together with the CCD pixel geometry and will allow us to verify the pixel geometry even with the cover in place.

The focal length dependence of the wavelength is much more critical; e.g. a deviation of 50 nm produces a shift in focal length of about 4.3mm. Therefore, the light-attenuating filter in front of the CCD also serves the purpose of reducing the chromatic aberration. A two-stage reflective bandpass filter[15] (center wavelength at 670nm, 12nm FWHM wide, peak transmission 1.5%) was used: the narrow bandpass filter is coated on the lenses, while a filter blocking the regions far away from the bandpass is coated on a glass plate directly in front of the CCD. The latter ensures a safe reduction of the stray light that may pass through spurious leaks in the supposedly light-tight MLI cover of the whole imager tube. The glass plates are not parallel with the CCD plane in order to deflect the CCD reflected light away from the CCD. The coatings are ion-plated, currently the best procedure to obtain mechanically stable and dense coatings.

Due to diffraction and chromatic aberration the limb amplitude variation (from about 0% to about 50% of the Sun center intensity at 670nm)[16] is spread over about 3 pixels. This ensures a precise limb determination while still keeping the SAS telemetry rate in 'limb mode' at an acceptable level (~3kBytes/sec).

3.2.2.2. CCD, Mounting Structure, and Electronic Box

The CCD (Loral 145 EDC) contains 2048 square pixels of 13x13 μm^2 and is glued directly to an Al standoff, which is bolted to the rear grid tray to guarantee stable positioning. The standoff reaches through a rectangular hole in the PC board; therefore the position of the CCD is defined by the standoff not by the PC-board.

The CCD was operated under irradiation of 100MeV protons with periodic measurements of the dark signal (DS), the Sun-equivalent signal, and the offset level. We observed an increase of the dark signal after 11krad of 90mV and a potential decrease of the sensitivity by 15%. For the dose expected over 2 years in space (about 1.5krad) the DS increased by only 1mV. The CCD also survived the HESSI vibration level. Figure 6 shows a photograph of the open FM electronic box.

3.2.2.3. Front-End Electronics

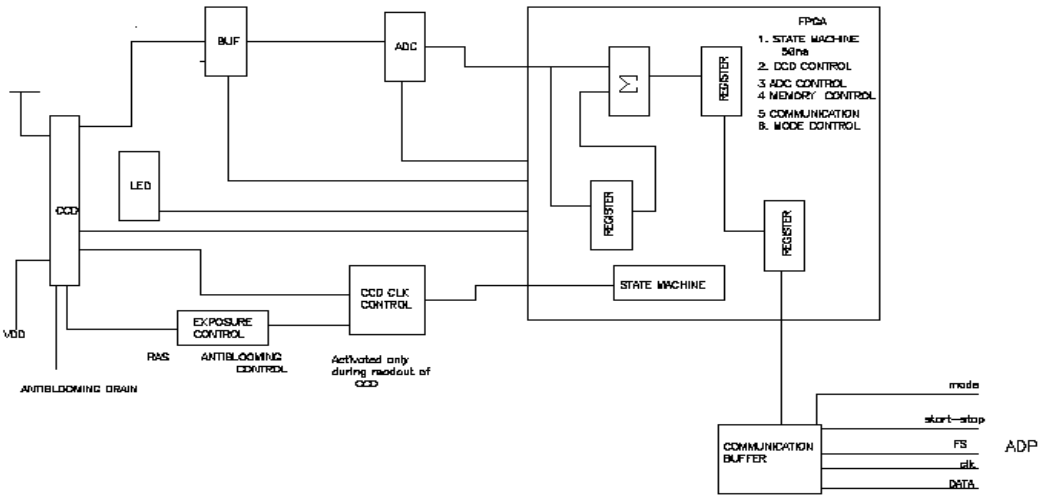

Figure 7: Block diagram of the SAS front-end PCP board (essentially identical to the RAS board).

A block diagram of the front-end electronic scheme is given in Figure 7. The main components are the CCD, a Field Programmable Gate Array (FPGA, Actel RH1020), an ADC, an LED for test purposes, and the necessary periphery. The FPGA provides all the necessary CCD and ADC control signals, reads the ADC and sends the data to transmission speed of 1μsec/pixel via a synchronous serial link. The ADP itself communicates with the Instrument Data Processing Unit (IDPU).

The readout cadency was fixed to 128Hz, corresponding to about 8msec. The CCD readout time t_R is about 2.1msec. Thus, for the typical integration time of around 0.5msec there are roughly 7.2msec during which the photosites are charged up. This is a non-recommended mode for the Loral 145 CDC, since the photosite charge is not completely drained to the reset drain during the long period between the end of the first and the beginning of the next integration time. The photosites are therefore still partly charged at the beginning of the next integration period. This behavior causes a drastically enhanced odd-even response, which is much higher than the specified 40mV. In general odd-even or register imbalance describe the fact that odd and even pixels have a different gain factor. Initial tests showed that this effect is reduced by using (a) the maximum cadency (128Hz) and (b) a pre-integration scheme. This means that the integration time t_{int} is preceded by a pre-integration (of fixed duration $t_1 = 0.002ms << t_{int}$), which completely removes the charge if the time t_{pre} between the end of the pre-integration reading and the beginning of the real reading is sufficiently small (< 0.03msec). The integration time t_{int} can be set between 0.016msec and 2msec in steps of 0.016msec. With this scheme and for $t_{int} > 0.3msec$ we observed small odd-even effects. Test measurements with a second pre-integration gave no significant improvement.

In order to improve the noise performance we implemented a Digital Correlated Double Sampling (DCDS) as outlined in Figure 8. The voltage signal of each pixel is sampled twice (at signal level and at offset level) and digitally converted to 12 bits. Both levels are then subtracted from each other resulting in a 10bit signal.

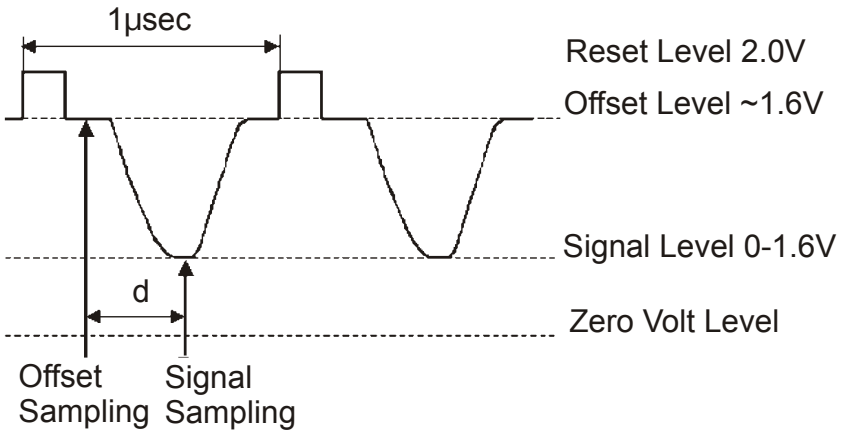

Figure 8: Schematic outline of the DCDS. The delay d between the two different samplings is 250ns (SAS) and 500ns (RAS).

The readout modes can be selected from the ADP and are given in Table 4:

Mode	Description
0	Normal mode: Signal - Offset, bits 1-10, 1mV/ch
1	Offset, 10 LSB, bits 0-9, 0.5mV/ch
2	Signal, 10 MSB, bits 2-11, 2mV/ch
3	Offset, bits 2-11, 2mV/ch
4	Stimulate LED (100% duty-cycle), bits 1-10, 1mV/ch
5	Stimulate LED (50% duty-cycle), bits 1-10, 1mV/ch
6	Communication test mode, 10 bit
7	Signal - Offset, running average over 2 pixels for on-board odd/even correction, bits 1-10, 1mV/ch

Table 4: Operation modes of SAS. In modes 4 and 5 an LED is activated for test purposes.

The power for SAS is delivered from the IDPU separately for +14V, +12V, +5V. The power consumption per SAS unit is 1.2W.

3.3. Roll Angle System (RAS)

3.3.1. Overview

The basic RAS principle is to determine the momentary RHESSI roll orientation with respect to known stars. In the rotating plane the roll angle determination can be reduced to a time determination. Since the starlight is focused onto the linear CCD for about 15msec, a high data rate of around 100Hz is the limiting requirements for the RHESSI RAS. Standard 2-d star trackers are optimized for high sensitivity and accurate position determination, usually achieved by long integration times, and hence not usable for our purpose. A 1-d scanner type with the required conditions of accuracy, low mass, power, and cost is commercially not available.

An independent RAS device with a photomultiplier instead of a CCD, is installed on the instrument for redundancy (for details see Ref. 17).

3.3.2. Requirements

The RAS accuracy is driven by the requirement that the nominal resolution should not be degraded by the uncertainty of the roll angle determination. To get some numerical estimate we take the mean displacement of typical Sun flares of ~ 13arcmin. This displacement and the 1arcmin uncertainty of the roll angle yields a comparatively small contribution

(0.2arcsec at a 1-σ level) to the image blur. The spacecraft pointing and the roll angle should be continuously available over time periods of up to 1000 sec to allow for long integrations in order to build up the momentary aspect solution for any photon observed. In order to provide precise correlation with other observations we must know the absolute roll angle to 1arcmin.

3.3.3. RAS: Principle of Operation

We define the RHESSI rotation angle as roll angle ϕ with the rotation axis pointing towards the Sun as the +z axis of the right-handed imager coordinate system. The xy-plane is hence called the roll angle plane. Furthermore, the plane formed by the momentary RAS pointing direction and the z-direction is called RAS image plane with the polar angle θ denoting the angle between the z-direction and any light ray imaged on the CCD. The RAS roll angle is determined by timing the detection of an identified star. The problem of angle determination is thus reduced to a time measurement. Furthermore the prediction of the corresponding star map is straightforward, since RHESSI is always pointing to the Sun.

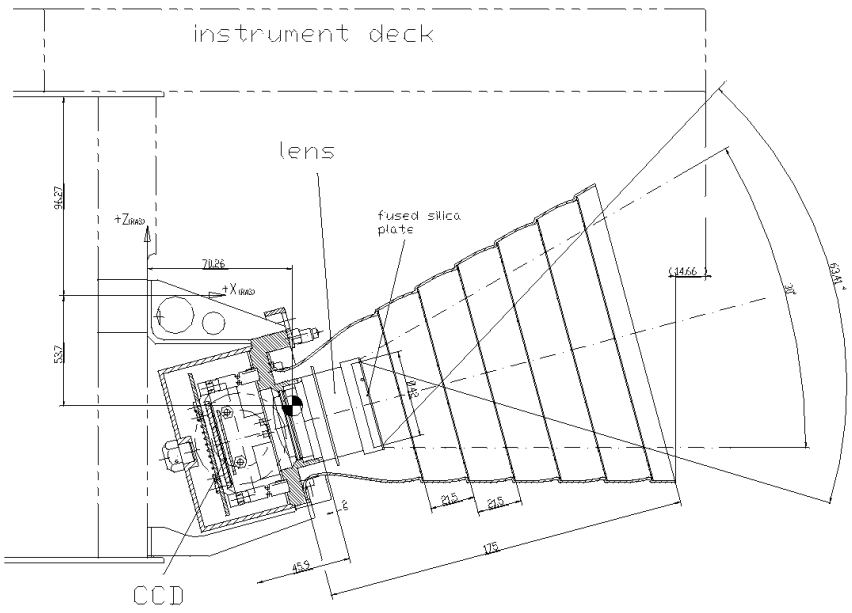

Figure 9: Cross-section of the RAS. The z-axis is pointing towards the Sun.

The RAS pointing direction was chosen at $\theta = 75°$ (see Figure 9) in order to reduce the length of the optical baffle. Stars within a field of view of $\theta_{FOV} = 30°$ by $\phi_{FOV} = 1.4°$ are focused by a 50mm lens onto a 2048-pixel linear CCD. The focal length translates into a pixel resolution of 0.9arcmin/pixel in the RAS image plane. The passage of a star image over the CCD perpendicular to the line of direction will stimulate a signal in one or in several pixels. During each passage of approximately 16.5msec duration we will measure typically three, strictly consecutive time frames with selectable integration time of typically 9msec. The determination of the crossing time, weighted with the measured amplitude, allows the reconstruction of the corresponding momentary roll angle for a given star by $\delta\phi = \delta t\, 2\pi/\tau$, (rotation period τ=4sec. Thus, in order to achieve the accuracy of 1arcmin we need a timing accuracy of $\delta t \sim 0.19$msec. Obviously, for amplitudes slightly above threshold, sampling statistics and noise will considerably affect timing accuracy. However, it can be recovered by observing the same object over many rotations. Roll angles at intermediate times are inferred by assuming uniform rotation.

We selected the 15MHz Dalsa IL F2 CCD (2048 x 96 pixels, each pixel is 13μm^2) which is normally operated in such a mode that all 96 pixels in a row are summed, thus creating a line CCD with an effective pixel size of 2048x1248μm^2. Using a f/1.4-lens, the maximum signal expected for on-axis pointing for a star with visual magnitude $m_V = 3$ varies

between 3.3 mV for spectral type B and 7.2mV for type M. Given the CCD noise level of about 0.35mV rms we thus obtain a signal-to-noise ratio between 10 to 20 for $m_V = 3$ stars. A threshold level of about 5 times the noise level appears acceptable in order to prevent excessive noise triggering. Vignetting as well as off-axis broadening of the image Point Spread Function (PSF) with the Leica Summilux f/1.4, 50mm lens is expected to lead to a loss of sensitivity per pixel of almost 10 at the edge of the field of view.

The RAS main characteristics are listed in Table 5.

Field of view [deg^2]	1.4 x 30
Lens	Leica Summilux 1.4/f 50mm
Sensor	Dalsa IL F2, (2048 x 96) pixels, each pixel (13 μ)^2
Signal resolution	10 bit
Frame time resolution [μs]	16
Plate scale	14.5 μ/arcmin
Pixel resolution in polar plane	0.9arcmin/pixel
Pixel resolution in roll angle plane	85.9arcmin/(96 pixel), corresponding to 16.5msec/(96 pixel) at CCD center
Update rate [Hz]	16 – 125
Integration time [ms]	8 – 62
Mass, incl. Baffle, support [kg]	1.5
Power consumption [W]	1.5
Operating modes	Full images, star event
Data rate (event mode, 2 stars/s)	0.4 kByte/s
Operating temperature [°C]	-20°C to +5°C
Radiation hardness	≥ 6krad protons
Full system noise	0.35mV, equivalent to about 290 e$^-$
Sensitivity [m_V for class B]	-2 to +3.5
Spectral sensitivity [nm]	400…1000
Roll angle accuracy (1σ)	~ 1arcmin
Polar angle accuracy (1σ)	< 1arcmin

Table 5: Summary of RAS main characteristics

3.3.4. Mechanical Configuration

The RAS is mounted below the RHESSI instrument deck (see Figure 9). It has a mass of 1.5kg. The walls of the electronic box provide radiation shielding. RAS is mounted on a central Ti structure, which is clamped to the satellite interface by three Ti struts. This ensures large thermal resistance and a stable angular position of the RAS with respect to the RHESSI imager tube. Figure 10 shows a photograph of the RAS FM. Its main elements are described below.

3.3.4.1. Lens

The lens is a commercial Leica Summilux, f/1.4, 50mm without aperture and focal length adjustment. It was assembled oil-free and using space-qualified adhesives. The lens vibration qualification of Leica is 100g shock and 5g sinusoidal between 10 and 2000Hz; their thermal qualification is from –25°C to +70°C. We have performed a vacuum test and a thermal cycling test (-50°C to +50°C) with no adverse effects. A 4mm thick fused silica plate in front of the first lens serves as protection against radiation. Lens glass samples were irradiated with 15krad total dose by 60MeV protons (about twice the dose expected behind the fused silica plate or the lens housing structure over three years), which resulted in some yellow-brown coloring barely visible to the eye. Image distortion was calculated as increasing toward larger angles, up to 0.2% at 15° off-axis.[18] Based on theoretical calculations the focal length should ideally be shifted by about -0.1mm such that the PSF is reasonably balanced over the FOV. Since the focal length critically depends on the spectrum of the incident light, the adjustment of the focal length was performed *in situ* by observing the variation of the image width of stars on the CCD as a function of focal length and position on the CCD. The lens displays considerable vignetting which means that at the maximum incidence angle of 15° the throughput of light is lower be a factor of two compared to on-axis angle.

3.3.4.2. Baffle

The optical system is protected against direct Sun illumination by the satellite instrument deck and against Earth-reflected light by an optical baffle for a viewing angle of $\theta \geq \pm 32°$ and $\phi \geq \pm 20°$ from the RAS optical axis. The baffle was designed for the specific case when RHESSI is located exactly between Sun and Earth, i.e. local noon. This situation requires a stray-light reduction of about $5 \cdot 10^{-7}$. The design (see Figure 9) is based on simple geometric arguments (see e.g. Ref. 19) and optimized by extensive calculations with the ASAP/ APART stray light codes, considering the full optical path through the lens as well as the narrow FOV (± 0.7°) in the roll direction. The resulting design features 6 vanes with oblong apertures, mounted in a cone with an opening angle of 30°. It nominally reduces the stray light to about 1.2nW/mm^2 or 20% of a $m_V = 3$ star. The calculations showed that the properties of the knife-edge rim of 50μm radius of the vane contributed 20% to the total reflectivity. It is therefore more critical than the total reflectivity inside the baffle, which was assumed to be 0.06.

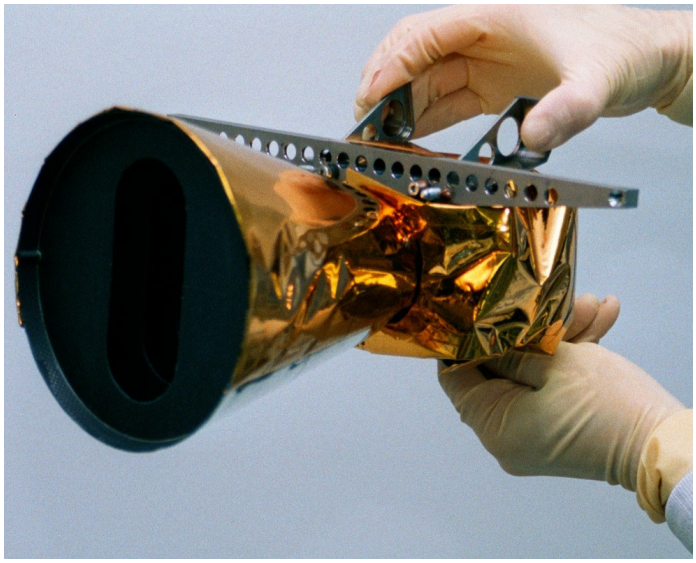

Figure 10: Photograph of the RAS FM. The two top support struts are visible above the electronic housing and behind the alignment bar with mounting cones for two tooling balls. Another tooling ball (not visible) is placed at the bottom of the central flange. Baffle length is 175mm and front vane diameter is 150mm.

For reasons of mass and mechanical stability the baffle was constructed with CFRP, containing a core of high-module fibers for thermal conductivity (κ= 600 W/m/K along the fiber direction) and covering layers of medium-module fibers for mechanical strength (M60J 3K/954-2A fabric from Hexcel Composites). Its overall thickness is about 1mm. The vanes are made of the medium-module fibers alone. They are 0.5mm thick with knife-edge rims of about 20μm radius at a 45° level.

Reflectivity measurements on several CFRP samples lifted off a microbead-blasted replica surface yielded a solar reflectivity of around 0.06,[6] which is only about 50% higher than special absorptive coatings. The baffle itself weighs about 150g.

The front vane, the bottom third of the baffle cone, and the bottom of the RAS electronic box are covered by silver-coated Teflon foil ($\alpha \sim 0.1$, $\varepsilon \sim 0.9$) to improve the radiative cooling to space. The thermal properties of the whole system were measured in the PSI thermal chamber for typical heat loads of the CCD and front-end electronics (1.5W). A CCD temperature of around -30ºC to -40ºC was obtained. The effective thermal conductivity of the composite baffle along the cone direction was evaluated at about 200W/m/K, i.e. similar to that of Al.

Thermal tests done with the fully integrated spacecraft at the 10-ft thermal vacuum chamber at JPL confirmed the thermal tests done at PSI. However, to ensure that a temperature above –30^{o}C is always maintained even in the non-operation mode, a bi-metal stabilized heater was installed with a turn-on point at –30^{o}C and a turn-off point at –20^{o}C.

3.3.4.3. Alignment Structures and RAS Pointing

RHESSI requires ± 1arcmin absolute roll angle knowledge with respect to the SAS and to each of the RMC systems. The alignment measurement was done after FM assembly. An artificial star (a LED illuminating a 0.5mm-diameter pinhole) was moved across the FOV at $\theta = 75°$ at two different distances from the lens. For each distance the centroid of the highly symmetric RAS response could be determined with an accuracy of 0.1arcmin. The pinhole positions were measured by theodolite triangulation with respect to the RAS and to the imager tooling balls, by which the RAS pointing direction is defined with respect to the imaging coordinate system.

The CCD polar angle setting was measured similar to the method described above, but with the LED pinhole moved at an off-axis angle of 13°. Determination of the corresponding centroid in the imager coordinate system yielded the CCD polar angle setting with arcminute accuracy.

Since the RAS pointing direction, as well as the SAS and grid geometries are measured in the imaging coordinate system, we can relate the RAS pointing direction directly to the SAS and the grids. An overall accuracy of 1arcmin. is obtained.

3.3.4.4. CCD Mounting Structure and Electronic Box

To ensure high-thermal conductivity and mechanical stability, the CCD and the CCD front-end PC-board are bonded directly to a solid aluminum structure that is clamped to the central Ti frame. A film heater is bonded on this structure close to the CCD and to the corresponding thermistor to allow for controlled thermal stabilization. The heater is covered by a grounded Al tape to reduce electromagnetic interference with the close-by electronic board. Two independent thermistors measure the temperature of the electronic housing.

The electronic box around the CCD card provides a light-tight housing and 2mm aluminum radiation shielding. Considering the RHESSI orbit and a 3-year lifetime, we tested the components with 8krad total dose by protons of 60MeV. For the CCD we observed a 20% increase of the dark level after 8krad.

A commercial one-time operated mechanical shutter directly in front of the CCD protects the CCD from accidental Sun illumination in the initial phase. The device (Ti-Ni Aerospace) operates on the principle of a loaded spring that is released by heating an actuator.

3.3.5. CCD and Front-End Electronics

The CCD was selected according to pixel geometry and readout speed. The concept to record several consecutive time frames of the same star required a linear CCD with pixels that are sufficiently extended into roll plane. We started out with the Dalsa IL C6, with a 2048-pixel CCD of 500x13 μm^2 -size pixel. However, large pixel size brings along high capacitance and, ultimately, unacceptably low charge-transfer efficiency. It was therefore replaced by the Dalsa IL F2, which is an almost pin-compatible two-dimensional device with 2048 x 96 pixels, of 13μm^2 each. In Time-Delayed-Integration (TDI) mode one can implement online binning over a certain fraction of the 96 pixels.

A block diagram of the electronic scheme is given in Figure 7. The CCD board contains the FPGA (Actel RH1020), which provides all necessary CCD and ADC control signals, reads the ADC and sends the data to the SAS/RAS Aspect Data Processor (ADP) with a transmission speed of 1μsec/pixel via a synchronous serial link. The ADP itself communicates with the Instrument Data Processing Unit (IDPU). It is described in Refs. 20, 21.

Since maximum sensitivity and thus low noise are the main requirements for the RAS, we implemented a DCDS, similar to the SAS described above (outlined in Figure 8), thus reducing the reset-noise component for frequencies below about 2MHz.

Table 6 indicates the RAS operation mode that can be selected from the ADP.

Mode	**Operation**
0	Normal mode: signal - offset, bits 0-9, 0.5mV/ch, 96 pixel binning
1	Normal mode: Signal-offset, bits 0-9, 0.5mV/ch, 48 pixel binning
2	Technical mode: increment of Earth-shine threshold counter
3	Technical mode: fast reading in Earth albedo mode
4	As mode 0, with stimulated LED, bits 0-9, 0.5mV/ch, 96 pixel binning
5	Signal only, 10 MSB, bits 2-11, 2mV/ch, 96 pixel binning
6	Offset only, 10 MSB, bits 2-11, 2mV/ch, 96 pixel binning
7	Data integrity test mode (‘saw tooth’), 10 bits and reset of Earth albedo threshold counter.

Table 6: RAS operation modes. In modes 4 an LED is activated for test purposes

Modes 0 and 1 are the standard data-taking modes, with mode 1 using 48-pixel binning instead of 96-pixel binning, which may result in an improved S/N if the star image movement can be synchronized with the integration time. Modes 2 and 3 are technical modes used in connection with the Earth albedo mode (see below). In mode 4 an LED positioned on the front side of the board close to the CCD is stimulated for 16μsec every 16th frame and its light measured for test purposes. Modes 5 and 6 are used to analyze signal and offset separately, and for redundancy.

The frame cycle time, which also corresponds to the integration time, can be selected in steps of 0.24msec between 8msec up to 52msec. The CCD readout time is essentially given by the transmission speed. It is about 2.2msec.

Since the Dalsa IL F2 has no anti-blooming provisions, the recovery time after exposure to very intense illumination like Earth albedo represented a major problem. After the periodic exposure to Earth-reflected sunlight (every 4sec for nearly 2sec with intensity as much as 1000 times the saturation level) the system should be nominally sensitive with a minimum dead time. Since the recovery time after deep saturation depends directly on the number of CCD readings, we implemented a special ES suppression circuit triggered by the sum of any 64 pixels over a selectable threshold. It activates reading with the shortest possible integration time of 2.2msec. Thus fast reading is maintained as long as the ES trigger is activated. When the ES trigger is no longer activated, fast reading is still maintained for a programmable period in order to make sure that all residual charge has been removed.

Filtered power is separately delivered from the IDPU for +14V, +12V, and +5V. Residual noise turned out to be very critical for the CCD noise performance and was sufficiently reduced by a filter close to the RAS. The total power consumption of RAS is 1.5W.

3.3.6. Operating and Data Handling

The ADP accomplishes the following two main data processing modes:

- the image mode where the full information (time, position and amplitude) of all 2048 pixels is formatted and stored
- the event mode where only the information characterizing single star event, namely one pixel address and the pixel amplitudes above threshold, and n pixel addresses below threshold, are formatted and stored.

The event mode is the preferred operating mode. However, the image mode can be activated for special purposes, e.g. for studying the dark-current signal. In practice, operate in event mode is periodically interspersing with images mode at a selectable duty cycle.

Organizing a sensitive and robust selection of star event represented a major S/W challenge, since there are only about 6msec available for this task. The processing of the three SAS sensors must also be handled at the same time. Field Programmable Gate Arrays (FPGA) located in the front-end processor of the ADP achieves the task. In a first step an algorithm compares the amplitude of each pixel to the corresponding value of the programmable threshold table. All pixels above threshold are marked as high and their positions are stored. Next, the event identification software looks for adjacent high pixels, which are then treated together as one event. In order to accommodate very low-amplitudes, wide events that might produce two high pixels separated by one or several low pixels, a special mode can be implemented that defines such structures as one event if the number of intervening low pixels is < 2N. About 30 to 50 events can be processed per frame, depending on the number of pixels involved and on the complexity of the image in question. Once an event has been identified in this way the frame time, and the addresses and amplitudes of the pixels above threshold are written to the ADP Fifo memory. For a proper subtraction of the dark-signal and fitting of the peak the corresponding data of 2N adjacent pixels on both sides are also included. A S/W option records the time frames before and after the trigger as well, optimal timing of the events. The ADP DSP program then stores the formatted data in the ADP Fifo memory from where it is read out by the IDPU via a communication FPGA.

Since a star image is typically spread over several pixels, summing over several pixels and comparing to a summation threshold table can increase the trigger sensitivity. Special pixel-summing schemes were implemented for this purpose:

(a) following the predicted variation[18] of the PSF as a function of the incident angle, the pixel range is subdivided into 5 sections where the amplitude summing is performed over a selectable number of pixels (2 to 4) in order to improve trigger efficiency.

(b) in addition, and independent of the spatial pixel summing, time-summation can be activated whereby the pixel amplitudes of two consecutive time frames are summed and compared to a special threshold table. Of course, spatial summation as well as time summation requires loading of special pixel-dependent threshold tables. Similarly as in the case without summation, all the single pixel amplitudes, addresses, and times, including 2N adjacent pixels and 2 adjacent time frames, are buffered for data transfer.

The data rate for 10 stars per rotation in event mode is about 0.5kbyte/s.

3.3.6.1. CCD Performance

Apart from checking the basic CCD parameters the main emphasis of the test measurements was on issues intimately related to the RAS application. The normal – and most demanding – operation mode in space will be the event mode.

Obviously, in order to optimize the sensitivity and at the same time keep the data rate acceptable, the following conditions should be optimized:

- Low noise, constant over pixel range and over time
- Stable dark signal (DS)

3.3.6.2. Circuit Optimization and Basic CCD Parameters

The temperature-dependent variation of the offset signal was measured to be within specification over the whole range -30℃ to +40℃. The saturation voltage was adjusted to 450mV, i.e. channel 900 in mode 0 (see Table 6), since the CCD response became increasingly non-linear above 450mV. This results in a dynamic range of 1300:1 at the noise rms value of 0.35mV.

3.3.6.3. Dark Signal (DS)

The dark signal is the output signal in the absence of light. It originates mainly from integrated leakage current and thermodynamic noise. Ideally, it should linearly depend on the integration time and on temperature in such a way that the DS doubles with a temperature increase $\Delta T \approx 6 - 8$℃. Figure 11 shows the temperature dependence of the assembled FM for different integration times. While at temperatures above zero the DS appears to follow the predicted behavior, it stabilizes below 0℃ at a level of about 16 to 17mV. At low temperature the DS is independent of integration time. However if the low temperature offset is subtracted from the results, the data at 30℃ become almost linear with integration time. Obviously, this points in the direction of a non-thermal DS contribution. It should be noted that for our application the residual DS is not critical as long as it does not exhibit temperature dependence, which is the case below 0℃. In-flight data show that RAS can be stabilized at -15°C without problems.

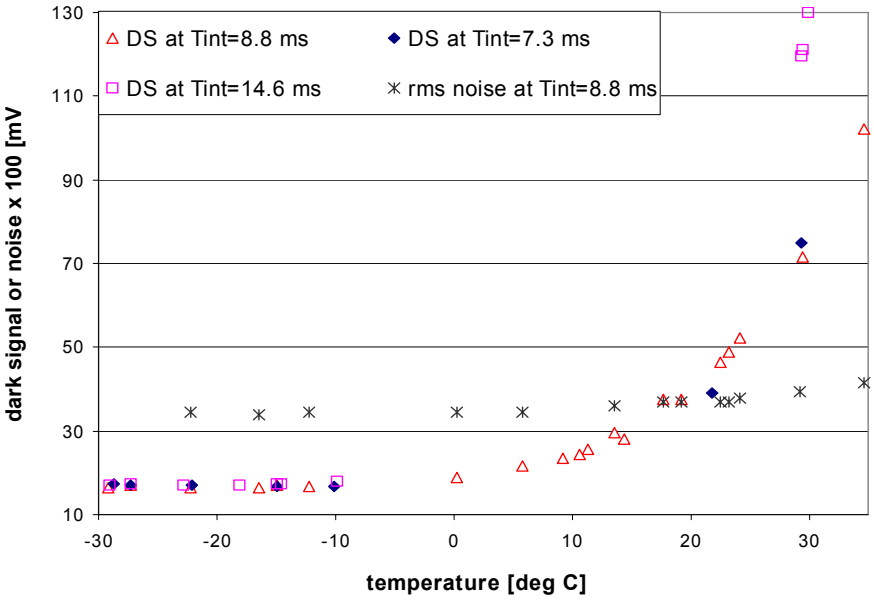

Figure 11: Dark signal (DS) and rms noise (*) (multiplied by 100) averaged over all pixels as a function of temperature.

3.3.6.4. Noise

The full system noise consists of the reset noise, the amplifier noise, the dark signal noise, the charge-transfer noise, the trapping noise, the fixed-pattern noise, the photon shot noise and the ADC digitization noise. Since the amplitude regime for operation is very close to the DS, we are mostly concerned about the first 5 noise sources and not so much about photon shot-noise and fixed-pattern noise, which only become dominant at larger amplitudes. Our DCDS effectively reduces the reset noise, and the individual pixel thresholding reduces the fixed-pattern noise. As seen in Figure 11, the noise appears to decrease in a manner similar to the DS, indicating a small noise component originating from the DS. The average noise at low temperatures of about 0.35mV is higher than the calculated value of 0.14mV given by Dalsa.[22] Note that we measured with an ADC resolution of 0.5mV/ch. The noise value corresponds to roughly 290e^- using a typical voltage-to-charge conversion factor of 1.2μV/e^- given by the output node capacity.

4. ENVIRONMENTAL QUALIFICATION OF THE IMAGER

The stability of the imager with regard to possible twist caused by environmental changes was our biggest concern, in particular temperature changes, outgassing of the CFRP tube in orbit, and mechanical forces exerted during transport and launch. Therefore thermal, vacuum and vibration test were performed for the imager before integration. Tests were repeated at spacecraft level at JPL, Pasadena. The TMS and the CMM at PSI were used for monitoring twists, if possible.

4.1. Thermal and Vacuum Tests

The assembled and aligned FM imager was repeatedly heated to + 40°C and cooled to about 0°C in a climate chamber at Contraves Space, Switzerland for thermal qualification. No significant twist has been measured using the TMS as with the QM imager before. Five thermal cycles were performed with the FM imager, first without and then with the grids mounted.

Outgassing was tested in vacuum using the QM tube. The geometry was measured with the CMM at PSI before and during the vacuum test. The shrinking was controlled and monitored in vacuum. After 3 months in vacuum, the coordinates of the front end-ring with respect to the rear end-ring showed the following changes: $\delta x=(0.047 \pm 0.016)$mm, $\delta y= (-0.003 \pm 0.016)$mm, and the shrinking $\delta z=(-0.056 \pm 0.014)$mm. The change in twist was $\delta\alpha=(-3 \pm 1)$arcsec, i.e. zero. Only shrinking was significant, decreasing exponentially ($0.048\ e^{-t/\tau}$ mm) with a shrinking time of $\tau=(23 \pm 3)$ days.

4.2. Vibration

Qualification and acceptance tests on the imager were performed based on the generic NASA requirements. The PSD loads used for the RHESSI qualification were derived by scaling these requirements to an imager mass of 57 kg: 0.0104 [g2/Hz] @ 20Hz, 0.0637 @ 50 – 800Hz, and 0.0104 @ 2000Hz with linear slopes in between. Before and after a random ± imager, which was also used for set-up tests before vibrating the FM.

During acceptance testing of the FM special care was taken not to over-test the delicate grids and their fragile mounts, therefore random force-limited vibrations were performed.

4.3. Gridlet Tests

A dedicated so-called gridlet end-to-end test was performed at PSI using GSFC equipment in order to gain totally independent verification of the correct alignment of the grids. The results were in excellent agreement with the TMS values.

4.4. Structural Stability of Imager after Mishap

In the course of the environmental tests of the fully assembled spacecraft at JPL (Pasadena), the structure was subjects to loads significantly exceeding qualification requirements, which damaged the spacecraft. The imager was brought back to Switzerland. Careful inspection revealed no severe damage to the hardware, only slight deformations of some tray and grid mounts were detected. After a complete disassembly the imager was reassembly with new mounts, aligned and brought back to a flight conditions within three months.

4.5. Transportation and Full System Environmental Test at JPL

The imager was integrated into the spacecraft at SSL in Berkeley in September 2000, followed by environmental tests at JPL in Pasadena and VAFB in Locum. After each transportation leg and test, a full TMS verify the twist stability of the grids and trays. The results (see Figure 12) show excellent stability of the whole system. The most stringent requirement of +- 20 arcsec for the finest grid collimator is well fulfilled. The TMS of the trays is the most precise due to its large size. It shows that the trays were stable to less than 5 arcsec, corresponding to less than 5 μm at the periphery.

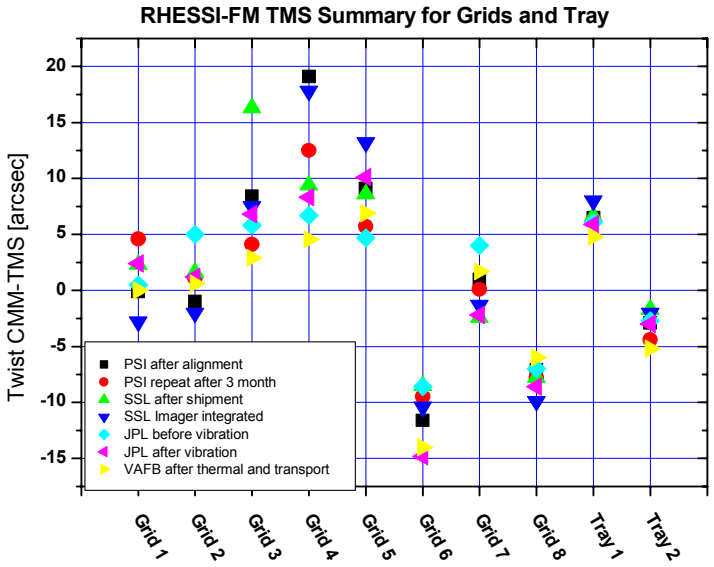

Figure 12: Summary of TMS measurements after transportation and environmental tests. Note the twist requirement for the finest grid is 20arcsec

4.6. In-Flight-Stability Verification.

The SAS allows for verification of any tray-to-tray twist after launch and operation in space (for details see Ref. 23). Again excellent stability was found (<3arcsec). Extensive simulation of the whole imager with the GEANT code using the CMM measurements for position of the grids, verified that the grid parameters[8] calibrated in-space agree to arcsec with the those deduced from ground-based CMM measurements.

5. CONCLUSION

It is shown, that a hard-X-ray imager with arcsecond image capability, which imposes stringent mechanical requirements and high-precision aspect systems, can be built and successfully operated in space.

6. ACKNOWLEDGEMENTS

We express our thanks to a large number of institutions and individuals. Special thanks go to ACE in Fredericia, Denmark, the Composites Laboratory in Berkeley, and ETH Bauweisenlabor in Zurich who produced the imager tube. The mechanical workshop, the transport and the purchasing department at PSI were of great help to accomplish RHESSI in due time. The project was supported by a grant from the Swiss National Science Foundation.

REFERENCES

1 R. P. Lin, G. J. Hurford, N. W. Madden, et al., "High-Energy Solar Spectroscopic Imager (HESSI) Small Explorer mission for the next (2000) solar maximum", C. M. Korendyke, *Proc. SPIE, Missions to the Sun II*, **3442**, pp. 2-12, 1998.

2 L. N. Mertz, G. H. Nakano, and J. R. Kilner, "Rotational aperture synthesis for X-rays", *A: Optics and Image Science*, **3**, pp. 2167-2170., 1986.

3 T. A. Prince, G. J. Hurford, H. S. Hudson, et al., "Gamma-ray and hard X-ray imaging of solar flares", *Solar Physics*, **118**, pp. 269-290, 1988.

4 D. M. Smith and H. Team, "The HESSI Spectrometer", *ASP Conference Series,* R. Ramaty and N. Mandzhavidze, **206**, 2000.

5 R. Henneck, J. Bialkowski, F. Burri, et al., "Solar Aspect System (SAS) for the High-Energy Solar Spectroscopic Imager (HESSI)", *Proc. SPIE, EUV, X-Ray, and Gamma-Ray Instrumentation for Astronomy X*, **3765**, pp. 771-776, 1999.

6 R. Henneck, J. Bialkowski, F. Burri, et al., "The Roll Angle System (RAS) for the High-Energy Solar Spectroscopic Imager HESSI", *Proc. SPIE, EUV, X-Ray, and Gamma-Ray Instrumentation for Astronomy X*, **3765**, pp. 518-523, 1999.

7 H. F. van Beek, P. Hoyng, B. Lafleur, et al., "The Hard X-ray Imaging Spectrometer HXIS", *Solar Physics*, **65**, pp. 39-52, 1980.

8 G. J. Hurford, "HESSI Imaging principle and error budget", to be published in *Solar Physics*, 2002.

9 HESSI Team, *HESSI, Small-Class Explorer Proposal AO-97-OSS-03*, Space Sciences Laboratory, Berkeley; Goddard Space Flight Center, Greenbelt; Paul Scherrer Institut, Villigen, 1997.

10 *ACE Internal Report to PSI*, ACE Fredericia, Denmark, 1998.

11 G. J. Hurford, "Grid Fabrication and Characterization", to be published in *Solar Physics*, 2002.

12 M. Fivian, J. Bialkowski, W. Hajdas, et al., "Calibrating the aspect systems of the High-energy solar spectroscopic imager (HESSI)", *Proc. SPIE, EUV, X-Ray, and Gamma-Ray Instrumentation for Astronomy X*, **4012**, pp. 518 - 523, 2000.

13 D. Amato, D. Pankow, and K. Thomsen, "Force limited vibration test of HESSI imager", Garmisch-Partenkirchen, Germany, 2000.

14 Fisba Optik AG, CH-9016 St. Gallen, Switzerland.

15 Dünnschicht-Technik Ing. H. Tafelmeier, D-83026 Rosenheim, Germany.

16 C. W. Allen, *Astrophysical Quantities* (The Athlone Press, London, 1973).

17 G. J. Hurford, "PMT RAS", to be published in *Solar Physics*, 2002.

18 M. Heiden, (private communication).

19 J. J. Arnoux, "Star sensor baffle optimization: some helpful practical design rules", *Proc. SPIE*, **2864**, pp. 333-338, 1996.

20 M. Fivian, Thesis ETH-Zurich, *to be published*.

21 D. Curtis, P. Berg, D. Gordon, et. al.,"The RHESSI Spacecraft Instrument Data Proceessing Unit', to be published in *Solar Physics*, 2002.

22 Dalsa, *CCD Databook*, 1996-1997.

23 M. Fivian and A. Zehnder, "RHESSI Aspect System and In-Flight Calibration", *SPIE Proceedings*, **4853**, pp. n.p., Waikoloa, Hawaii, 2002.